metals

MDPI

Article

Microstructure Evolution and Biodegradation Behavior of Laser Rapid Solidified Mg–Al–Zn Alloy

Chongxian He [1,†], Shizhen Bin [2,†], Ping Wu [3], Chengde Gao [1], Pei Feng [1], Youwen Yang [1], Long Liu [1], Yuanzhuo Zhou [1], Mingchun Zhao [4], Sheng Yang [5] and Cijun Shuai [1,6,7,*]

1 State Key Laboratory of High Performance Complex Manufacturing, Central South University, Changsha 410083, China; hechongxian@csu.edu.cn (C.H.); gaochengde@csu.edu.cn (C.G.); fengpei@csu.edu.cn (P.F.); yangyouwen@csu.edu.cn (Y.Y.); liulong@csu.edu.cn (L.L.); zyz420357155@csu.edu.cn (Y.Z.)
2 Department of Oncology, Third Xiangya Hospital of Central South University, Changsha 410013, China; shizhenbin@csu.edu.cn
3 College of Chemistry, Xiangtan University, Xiangtan 411105, China; pingwu@xtu.edu.cn
4 School of Material Science and Engineering, Central South University, Changsha 410083, China; mczhao@imr.ac.cn
5 Human Reproduction Center, Shenzhen Hospital of Hongkong University, Shenzhen 518053, China; tobyys2000@aliyun.com
6 Key Laboratory of Organ Injury, Aging and Regenerative Medicine of Hunan Province, Changsha 410008, China
7 State Key Laboratory for Powder Metallurgy, Central South University, Changsha 410083, China
* Correspondence: shuai@csu.edu.cn; Tel.: +86-731-8480-5412; Fax: +86-731-8887-9044
† These authors contributed equally to this work.

Academic Editor: Daolun Chen
Received: 2 February 2017; Accepted: 20 March 2017; Published: 22 March 2017

Abstract: The too fast degradation of magnesium (Mg) alloys is a major impediment hindering their orthopedic application, despite their superior mechanical properties and favorable biocompatibility. In this study, the degradation resistance of AZ61 (Al 6 wt. %, Zn 1 wt. %, remaining Mg) was enhanced by rapid solidification via selective laser melting (SLM). The results indicated that an increase of the laser power was beneficial for enhancing degradation resistance and microhardness due to the increase of relative density and formation of uniformed equiaxed grains. However, too high a laser power led to the increase of mass loss and decrease of microhardness due to coarsened equiaxed grains and a reduced solid solution of Al in the Mg matrix. In addition, immersion tests showed that the apatite increased with the increase of immersion time, which indicated that SLMed AZ61 possessed good bioactivity.

Keywords: AZ61; selective laser melting; microstructure; biodegradation behavior

1. Introduction

Mg alloys are potential degradable biomaterials due to their biodegradability, biocompatibility and a high specific strength [1–3]. Compared with other Mg alloys, Mg–Al–Zn alloys have received considerable attention as biodegradable metals due to their superior mechanical properties, relatively high degradation resistance and favorable biocompatibility [4,5]. However, the traditional methods of preparing Mg–Al–Zn alloys such as casting might lead to grain coarsening and component segregation due to their slow solidification rate.

Laser treatments, including laser surface melting (LSM), selective laser surface melting (SLSM) and selective laser melting (SLM), are effective methods to refine grain and homogenize the microstructure of Mg alloys. Among them, LSM is a surface modification technique, which consists in irradiating

surface of Mg alloys with enough energy to melt their external part [6]. Thus, LSM process can refine the microstructure and dissolve the second phase on the surface. These microstructure changes can improve the corrosion behavior of Mg alloys [7]. SLSM melts the β-phase without modifying the α-matrix [8]. These changes might promote the formation of micro-galvanic couples between the α-matrix and the laser modified β-phase. Meanwhile, the laser modified β-phase might form a closed network, which can imply a protective barrier against the corrosion attack [8].

In comparison, SLM is an additive manufacturing (AM) technology, enabling the manufacturing of parts directly from metal powders [9]. In addition, it has a cooling rate above 10^4–10^5 K·s^{-1}, which can interrupt the growth of grain [10]. Moreover, grain refinement by SLM can be achieved in the overall alloys, instead of the surface of alloys. The grain refinement has a significant enhancement of degradation resistance [11]. Furthermore, the rapid solidification also reduces the constituent segregation, contributing to forming a homogenously dispersed microstructure [12]. Moreover, it can extend the solid solubility of alloying elements in the matrix and reduce the formation of the intergranular phase, which restricts the local galvanic corrosion [13].

At present, SLM has been mainly concentrated on steel, titanium and so on [14–16]. Only a small amount of literature on using SLM to fabricate Mg alloys has been published. Ng et al. [17] have studied the single-track formation of pure Mg. They found that the width and height of single track are consistent though the laser energy changes. Wei et al. [18] have studied the effect of energy input on formability, microstructure and mechanical properties of selective laser melted AZ91D magnesium alloy. However, they were no research on how laser parameters affect degradation behavior of SLM Mg alloys.

In this paper, the influences of laser power on formability, microstructure, mechanical properties and degradation behavior of AZ61 were evaluated. In addition, the apatite layer deposition ability was identified by immersing the samples in simulated body fluid (SBF).

2. Materials and Methods

2.1. Material

Spherical AZ61 powder with a mean particle size of 70 μm was obtained from Tangshan Weihao Materials Co., Ltd. (Tangshan, China). Its X-ray diffraction (XRD) pattern and typical morphology were shown in Figure 1.

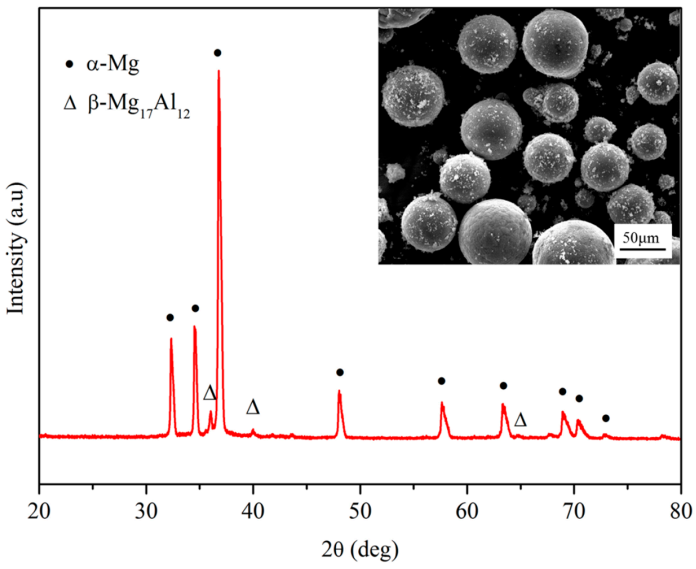

Figure 1. The X-ray diffraction (XRD) pattern and scanning electron microscopy (SEM) image of AZ61 powder.

2.2. Processing

SLMed AZ61 was prepared by a homemade laser melting system, which consisted of a fiber laser, an optical focusing system, a control system and a building platform. The detailed information could be seen in [19]. All the samples were fabricated in an argon atmosphere. After a series of pre-experiments, the scanning speed was set at 200 mm·min^{-1}, and the laser power ranged from 10 to 110 W. The other processing parameters: laser spot size 150 μm, layer thickness and hatch spacing 50 μm. Cubic samples with a size of 10 × 10 × 5 mm^3 were built.

2.3. Microstructure and Mechanical Characterization

The SLMed AZ61 was ground and polished, and then dried in a drying cabinet at 40 °C for 6 h. The metallographic microstructures of the samples were observed using an optical microscopy (PMG3, Olympus Corporation, Tokyo, Japan), and the grain sizes were measured by the intercept method [19]. The phase composition was analyzed by XRD (Rigaku, Hashima, Japan) using Cu Kα radiation (14 mA, 30 kV) with 2θ = 20°–80° at the rate of 10°·min^{-1}. The surfaces were characterized by a scanning electron microscopy (SEM) (Tescab Co., Brno, the Czech Republic) at an accelerating voltage of 10 kV. In addition, the microstructure and chemical distribution were detected by an energy dispersion spectrometry (EDS) (Jeol JSM5910LV, Tokyo, Japan) at accelerating voltage of 20 kV.

Relative densities of SLMed AZ61 were measured by using the Archimedes' method [20]. In addition, its microhardness tests were examined using a microhardness tester (Shanghai Taiming Optical Instrument Co. Ltd., Shanghai, China) at a loading force of 2.45 N and a holding time of 15 s.

2.4. Immersion Measurements

The in vitro immersion test was examined at 36.5 ± 0.5 °C in a simulated body fluid (SBF), which was prepared according to [21], and the composition was as followed: Na^+ 142.0 mM, K^+ 5.0 mM, Ca^{2+} 2.5 mM, Mg^{2+} 1.5 mM, Cl^- 147.8 mM, HCO_3^- 4.2 mM, HPO_4^{2-} 1.0 mM, and SO_4^{2-} 0.5 mM. The section parallel to deposition direction of SLMed AZ61 samples were ground and polished, and then dried in a drying cabinet at 40 °C and then weighed on the electric balance (EP225SM-DR, Precisa, Bern, Switzerland). Then, the samples were immersed in SBF for 144 h. At a different time point, the samples were removed from SBF, washed with absolute ethyl alcohol, dried in warm flowing air and immersed in a solution comprising 200 g·L^{-1} CrO_3 and 19 g·L^{-1} $AgNO_3$ for 10 min to remove the corrosion products. After that, they were quickly cleaned with distilled water, dried in warm flowing air and weighed for the final weight (mass loss = (mass before immersion−mass after cleaning in chromic acid)/surface area). The hydrogen evolution volume was also used to assess the degradation rate, and the surface and the chemical compositions of samples after immersion were studied using SEM.

2.5. Statistical Analysis

Statistical analysis was performed to assess the difference in grain size, relative density, microhardness and mass loss by the analysis of variance. Furthermore, the statistical significance was considered for $p < 0.05$ (significance level).

3. Results and Discussion

3.1. Formability

The formability of SLMed AZ61 on the section parallel to deposition direction was divided into four zones in the given scanning speed after a series of laser melting experiment (Figure 2). In zone A, the powders partially melted due to too low a laser power under 30 W (Figure 2a). In zone B, a ball-like structure appeared on the SLMed AZ61 when laser power was between 30 and 60 W (Figure 2b). It was believed that insufficient laser power led to the incomplete formation of the liquid phase and a consequent high viscosity of the solid–liquid mixture. This hindered the flow of the liquid and

rearrangement of the particles. As a result, the overall rheology of the liquid to solid particle binding performance was significantly lowered, causing the molten materials to aggregate into balls [22]. In zone C, SLMed AZ61 was dense when laser power was between 60 and 90 W (Figure 2c). However, in zone D, the melted powders evaporated away when laser power was above 90 W, resulting in the failure of the SLM experiment. As the forming zone of SLMed AZ61 was between 60 and 90 W, it was selected to study further.

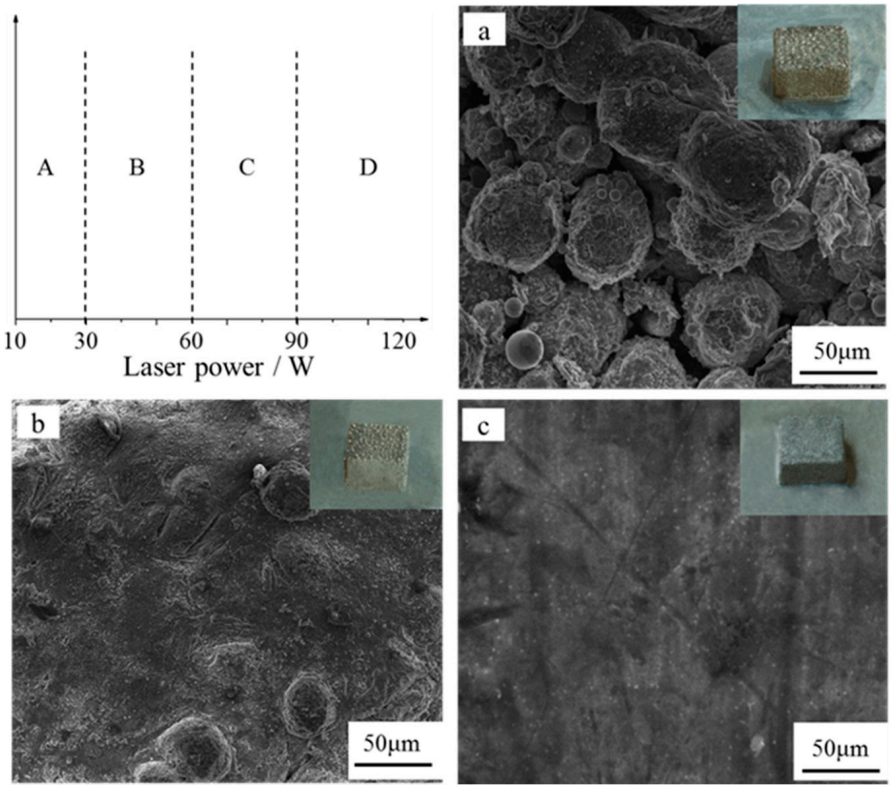

Figure 2. Formability of selective laser melted (SLMed) AZ61 at different laser power: (**a**) 20 W, zone A; (**b**) 50 W, zone B; (**c**) 70 W, zone C.

3.2. Microstructure Characterization

The microstructures of SLMed AZ61 on the section parallel to deposition direction at different laser power in zone C were presented in Figure 3. Furthermore, relative density and the grain size were shown in Figure 4. At laser power of 60 W, there were large numbers of irregular pores and fine dendrites (~5 μm) (Figure 3a), and the relative density was only 76% (Figure 4). As the power increased to 70 W, the amount of pores declined (Figure 3b) and the relative density increased to 88% (Figure 4). With increasing power to 80 W, the relative density of SLMed AZ61 increased to 98%, and it had uniformly equiaxed structure (~10 μm). However, as the power further increased to 90 W, the equiaxed grains were significantly coarsened (~14 μm) (Figure 3d).

The formation of pores (Figure 3a,b) was believed to be caused by the high dynamic viscosity of the liquid phase. The high dynamic viscosity hindered the liquid from spreading out. At laser power 80 W, SLMed AZ61 was dense. As the power further increasing to 90 W, the temperature of the molten pool was significantly increased, leading to prolonged cooling time [17]. As a result, the time for grains growing prolonged, and thus the grains were significantly coarsened (Figure 3d).

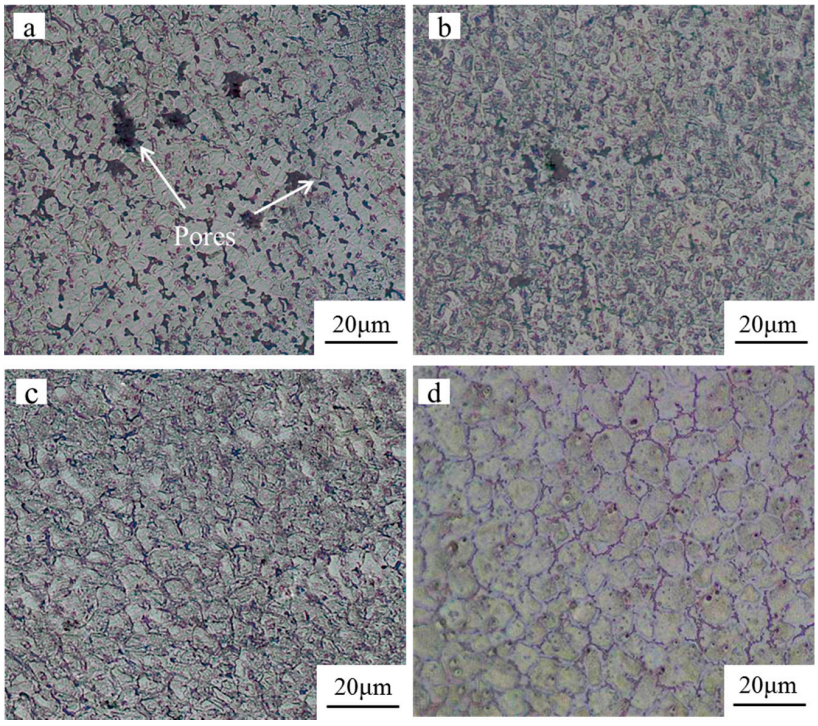

Figure 3. Optical images showing microstructure characteristic of SLMed AZ61 fabricated at different laser power: (**a**) 60 W; (**b**) 70 W; (**c**) 80 W; (**d**) 90 W.

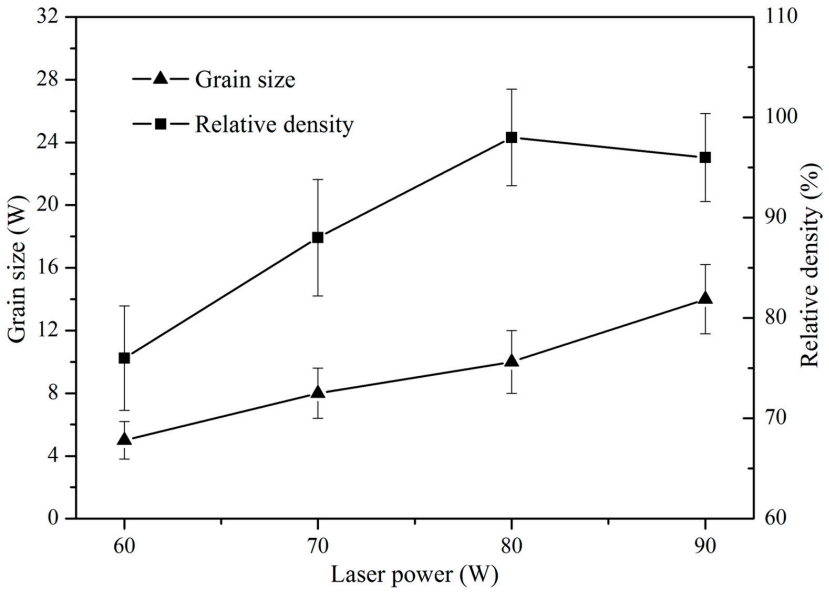

Figure 4. Grain size and relative density of SLMed AZ61 at different laser power.

3.3. Phase and Dispersion

The XRD results of SLMed AZ61 were shown in Figure 5a. It was revealed that SLMed AZ61 was composed of α-Mg and β-$Mg_{17}Al_{12}$. To analyze the XRD patterns accurately, a magnification view of the XRD patterns was shown in Figure 5b. In comparison with the standard α-Mg phase peak location (36.618°) [23], the α-Mg phase diffraction peaks location of SLMed AZ61 obviously shifted to high angles. Since atomic radii of Al (0.1199 nm) was 89.95% of Mg (0.1333 nm), Al acted as a substitutive solute in the α-Mg according to the theory of solid solution [24]. The incorporation of Al atoms into the

α-Mg led to the lattice distortion, which increased the lattice parameter of the α-Mg [25]. Therefore, the α-Mg diffraction peaks shifted to high angles. It was worth noticing that the offset of α-Mg diffraction peaks decreased as the laser power increased.

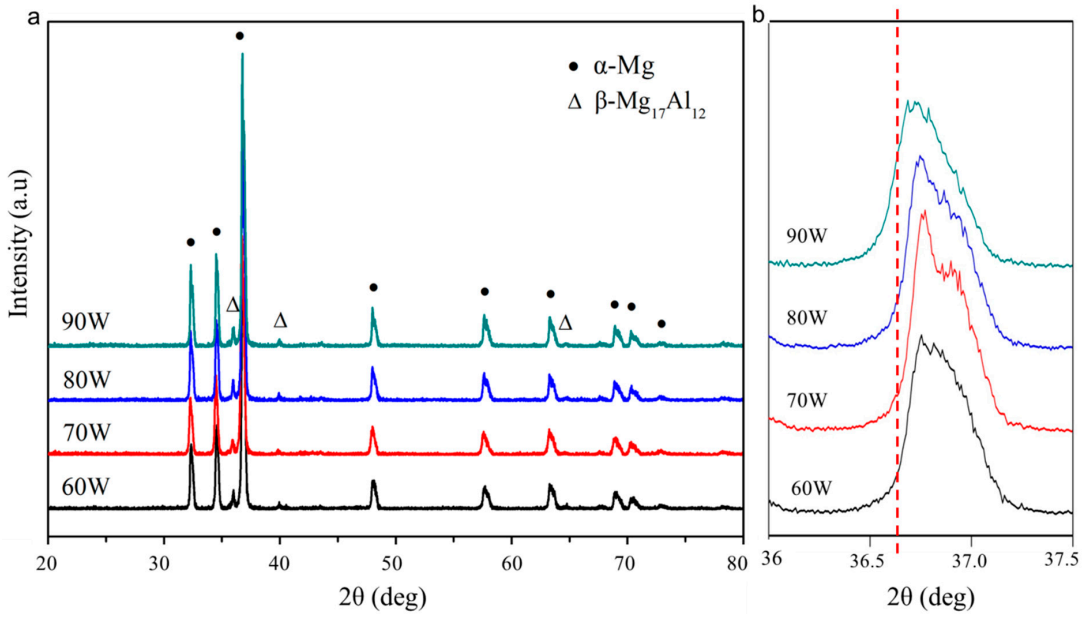

Figure 5. (**a**) The XRD pattern of SLMed AZ61 at different laser power; (**b**) details at angle range of 2θ = 36–37.5°. The red dashed line in (**b**) is the standard α-Mg phase peak location (36.618°).

The composition of SLMed AZ61 was further analyzed using SEM and EDS (Figure 6). For SLMed AZ61, the section parallel to deposition direction was taken into account. The SLMed AZ61 was consisted of the equiaxed α-Mg (gray regions) and discrete β-$Mg_{17}Al_{12}$ (bright regions). It was well known that the concentration of Al dissolved in the α-Mg affected not only the mechanical strengh but also the degradation resistance of the alloy [5,26]. For each samples, ten points in gray regions were selected to measure the solid solubility of Al in the α-Mg. In addition, the mean value of them was shown in the table. The Al content in the α-Mg decreased from 7.45 to 3.28 wt. % with increasing laser power from 60 to 90 W. Accroding to quantitative stereology, the surface fraction of α-Mg covered by β-$Mg_{17}Al_{12}$ of the SLMed AZ61 was considered to be equivalent to the area percentage of bright regions in tested sections. Furthermore, an Image-Pro Plus 6.0 software (Media Cybernetics, Rockville, MD, USA) was utilized to analyze the surface fraction. The area fraction of α-Mg covered by β-$Mg_{17}Al_{12}$ in each micrograph was determined by calculating the area ratio of the marked regions to the whole micrograph with the help of the statistics function. The surface fraction of β-$Mg_{17}Al_{12}$ was determined by counting the average area percentage of bright regions. Furthermore, the fitting function of surface fraction with laser power was:

$$y = 0.171x - 6.95, \quad (1)$$

where x was the laser power (W), and y was the surface fraction of α-Mg covered by β-$Mg_{17}Al_{12}$ (%). The surface fraction increased from 3.4% to 8.43% with increasing laser power from 60 to 90 W. Furthermore, the function of the evolution of surface fraction of α-Mg covered by β-$Mg_{17}Al_{12}$ with laser power was shown in Figure 6e. This could be explained by the effect of "solute trapping" [27], which was, in the solidification process of laser melting, solute atoms were overtaken by the advancing solidification interface and incorporated into the solid. As the laser power increased, the longer cooling time was required, which led to a weakening of the "solute trapping". Thus, the concentration of Al in α-Mg decreased with the increase of laser power. Moreover, the diffusion time of Al was insufficient so

that the "solute trapping" phenomenon in the α-Mg appeared and the formation of Al-rich β-$Mg_{17}Al_{12}$ phase was inhibited to some extent. The amount of β-$Mg_{17}Al_{12}$ precipitated with the increase of the laser power showed a rising trend, which would significantly decrease the degradation resistance of SLMed AZ61.

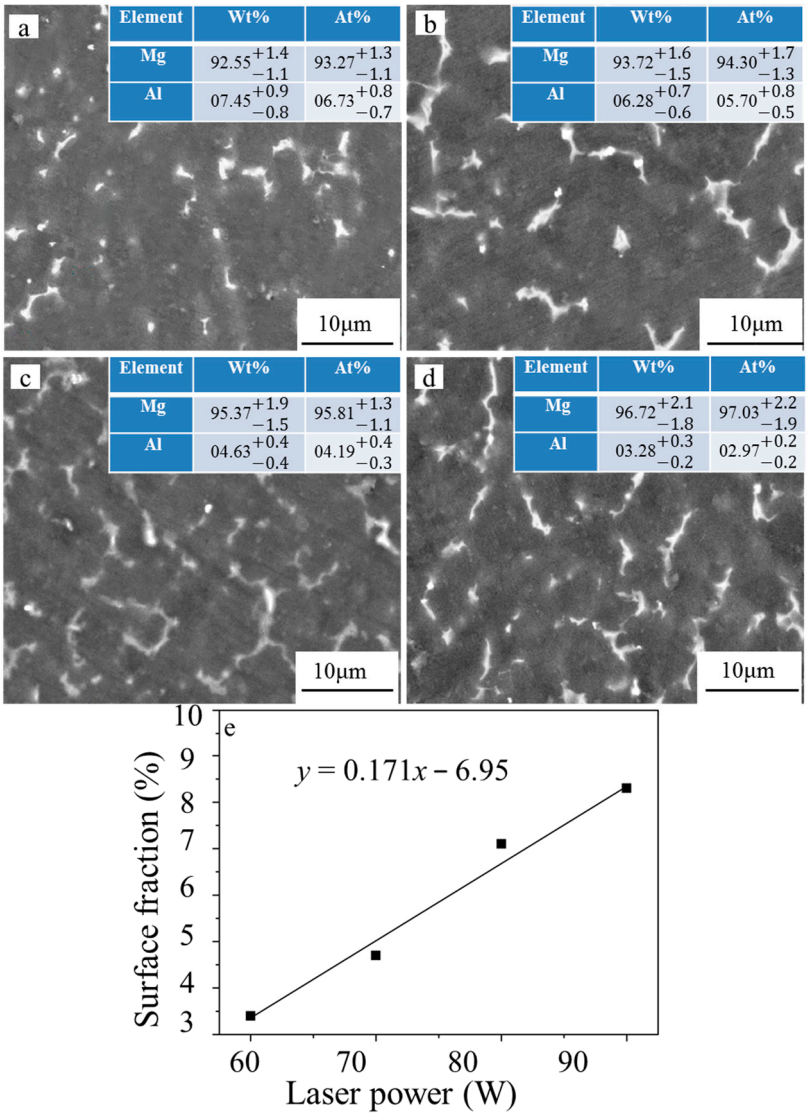

Figure 6. SEM and energy dispersion spectrometry (EDS) images of SLMed AZ61 at laser power of (**a**) 60 W; (**b**) 70 W; (**c**) 80 W; (**d**) 90 W; (**e**) surface fraction of α-Mg covered by β-$Mg_{17}Al_{12}$ as a function of laser power.

3.4. Microhardness

The microhardness of SLMed AZ61 was shown in Figure 7. Microhardness was taken once every 200 μm on cross section. At a laser power of 60 W, SLMed AZ61 exhibited low microhardness of 69.34 Hv. As laser power increased to 80 W, the microhardness gradually increased to 93.00 Hv. The increase of microhardness was attributed to the increase of relative density, with laser power increasing appropriately. However, upon further increasing laser power to 90 W, the microhardness decreased to 90.19 Hv. It was believed that grain refinement had a dominant effect on enhancing the mechanical properties of Mg alloys [28]. Therefore, the decrease of microhardness was attributed to the grain coarsening at an excessive laser power, as previously mentioned in Figure 3.

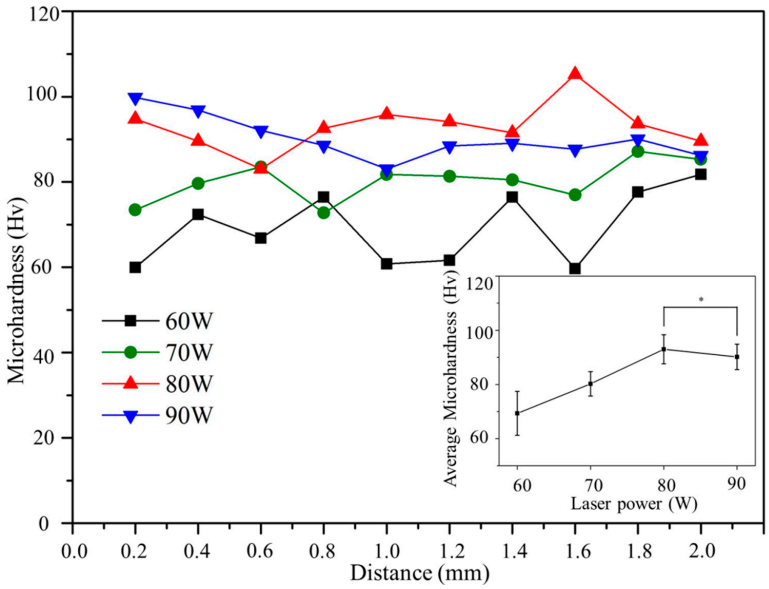

Figure 7. Microhardness of SLMed AZ61. Significant difference of average microhardness between 80 and 90 W (* $p < 0.05$).

3.5. Degradation

The degradation rate of SLMed AZ61 in SBF was calculated (Figure 8), and the corresponding degradation rate could be calculated via Equation [29]:

$$DR = \frac{W}{A\ T\ \rho}, \tag{2}$$

where DR was the degradation rate (mm·year^{-1}), W was the mass loss (g), A was the exposure area (cm^2), T was the exposure time (h) and ρ was the density (g·cm^{-3}). At laser power of 60 W, the AZ61 had the degradation rate of about 4.1 mm·year^{-1} after immersion for 24 h, and then decreased to 2.7 mm·year^{-1} after immersion for 144 h. Minimum degradation rate occurred at 80 W, whose value corresponding to 24 and 144 h was about 2.4 and 1.2 mm·year^{-1}, respectively. However, as power increased to 90 W, the degradation rate after immersion for 144 h was 1.5 mm·year^{-1}.

There existed some pores in SLMed AZ61 fabricated at 60 W, which might exacerbate its degradation. When the power reached to 80 W, the pores disappeared and the relative density of SLMed AZ61 became high. However, as the power further increased to 90 W, the mass loss increased. This could be explained by grain coarsening and solid solubility reduction, and the details were discussed as follows. The grain boundaries exposed after the α-Mg was etched acted as corrosion barriers; hence, fine grain size created more grain boundaries. Furthermore, fine grain size could form a denser surface oxide film, which provided better surface coverage for preventing ingress of Cl^- in the SBF solution. On the other hand, the solid solubility of Al in the α-Mg was affected by the "solid trapping", which reduced the formation of β-$Mg_{17}Al_{12}$ phase. Concerning the galvanic corrosion between α-Mg and β-$Mg_{17}Al_{12}$, an increase of Al in the α-Mg reduced the formation of β-$Mg_{17}Al_{12}$, which reduced the coupling effect and enhanced the degradation resistance of SLMed AZ61 [30].

The surfaces of SLMed AZ61 fabricated at 80 W after immersion for different times in Figure 9. With the increase of immersion time, the degradation products became thick and the cracks were wide. The formation of cracks was ascribed to the drying of the degradation products [31]. EDS analysis results (Figure 9e) showed the degradation products consisted of calcium, phosphorus, magnesium and oxygen. The Ca/P molar ratio was 1.69, which was close to 1.67 for hydroxyapatite, indicating certain apatite-forming ability.

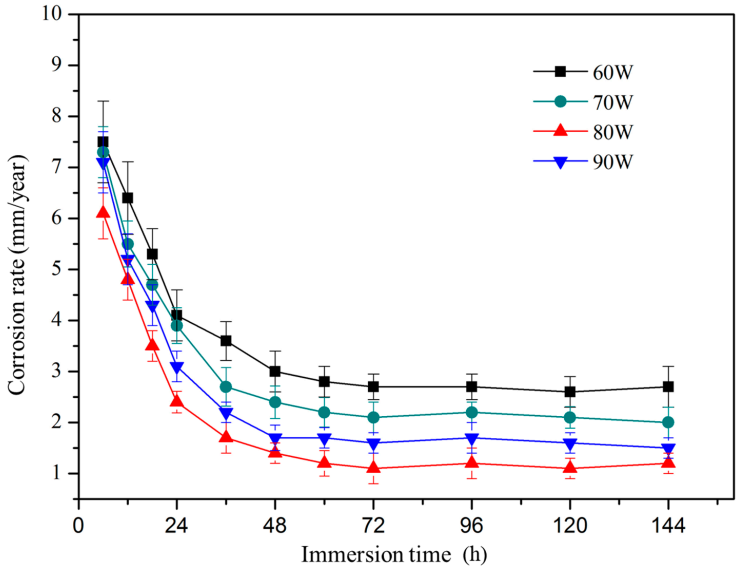

Figure 8. Degradation rate of SLMed AZ61.

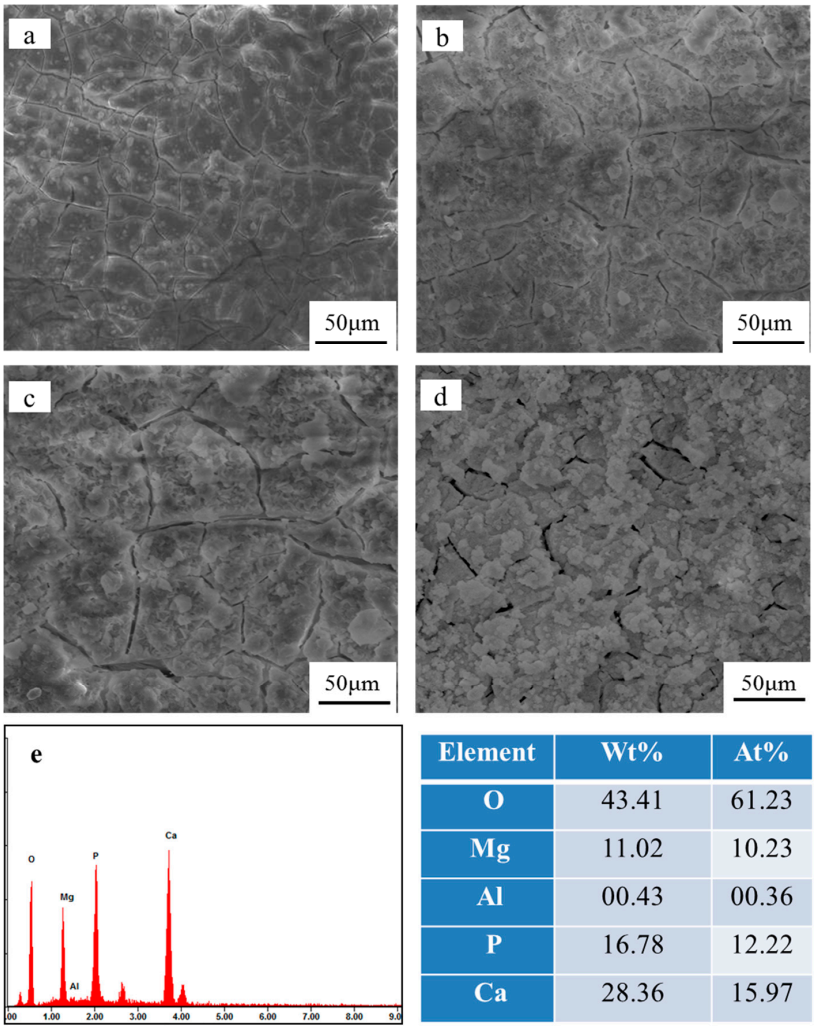

Element	Wt%	At%
O	43.41	61.23
Mg	11.02	10.23
Al	00.43	00.36
P	16.78	12.22
Ca	28.36	15.97

Figure 9. SEM images of SLMed AZ61 after immersion for different times: (**a**) 24 h; (**b**) 48 h; (**c**) 96 h; (**d**) 144 h and (**e**) EDS analysis results of (**d**).

Mg degradation reactions in SBF usually reacted by an electrochemical reaction with water. The metal Mg was transferred into $Mg(OH)_2$ film. The degradation of Mg was accompanied with the hydrogen evolution reaction.

The main reaction of the degradation of Mg in SBF:

$$Mg + 2H_2O \rightarrow Mg(OH)_2 + H_2 \uparrow. \quad (3)$$

The reaction above would result in the increase of SBF pH value. Particularly, the concentration of OH^- around the immersion area was significantly increased. In addition, the following reactions occurred:

$$H_2PO_4^- + 2OH^- \rightarrow PO_3^- + 2H_2O, \quad (4)$$

$$HPO_4^{2-} + OH^- \rightarrow PO_4^{3-} + H_2O. \quad (5)$$

The PO_4^{3-} in SBF will bond with Ca^{2+} and Mg^{2+} to form the compound of hydroxyapatite and magnesium phosphate [32]. The undissolved $Mg(OH)_2$ film on the surface of Mg alloy was considered to provide beneficial sites for hydroxyapatite nucleation [31]. Consequently, lots of hydroxyapatite nuclei were formed on the surface and then hydroxyapatite would grow spontaneously by consuming the calcium and phosphate ions from the SBF.

4. Conclusions

The forming zone of SLMed AZ61 was between 60 and 90 W. The metallographic structure of SLMed AZ61 changed from finer dendrites to uniformed equiaxed grains as the power increased to 80 W. However, equiaxed grains significantly coarsened at a further increased power. SLMed AZ61 fabricated at 80 W had a minimum mass loss of 12.26 $mg \cdot cm^{-2}$ after immersion for 144 h and maximum microhardness of 93.00 Hv. In addition, SLMed AZ61 exhibited apatite-forming ability in SBF.

Acknowledgments: This work was supported by the following funds: (1) the Natural Science Foundation of China (51575537, 81572577); (2) Overseas, Hong Kong and Macau Scholars Collaborated Researching Fund of the National Natural Science Foundation of China (81428018); (3) Hunan Provincial Natural Science Foundation of China (14JJ1006, 2016JJ1027); (4) the Project of an Innovation-Driven Plan of Central South University (2015CXS008, 2016CX023); (5) the Open-End Fund for the Valuable and Precision Instruments of Central South University; (6) the fund of the State Key Laboratory of Solidification Processing in NWPU (SKLSP201605); (7) the fund of the State Key Laboratory for Powder Metallurgy; and (8) the Fundamental Research Funds for the Central Universities of Central South University.

Author Contributions: Cijun Shuai and Chengde Gao conceived the idea of enhancing the degradation resistance of Mg–Al–Zn alloy by laser rapid solidification. Pei Feng, Youwen Yang and Ping Wu designed the experiments. Shizhen Bin and Chongxian He prepared the alloy samples, analyzed the formability and the microstructure of SLMed AZ61. Yuanzhuo Zhou and Long Liu carried out the phase and dispersion of SLMed AZ61. Mingchun Zhao and Sheng Yang analyzed the microhardness and degradation of SLMed AZ61. All of the authors discussed the results and reviewed the manuscript.

Conflicts of Interest: The authors declare no conflict of interest.

References

1. Song, G. Control of biodegradation of biocompatable magnesium alloys. *Corros. Sci.* **2007**, *49*, 1696–1701. [CrossRef]
2. Virtanen, S. Biodegradable Mg and Mg alloys: Corrosion and biocompatibility. *Mater. Sci. Eng. B* **2011**, *176*, 1600–1608. [CrossRef]
3. Jemimah, W.; Shaylin, S.; Woodfield, T.B.F.; Staiger, M.P.; Dias, G.J. Magnesium biomaterials for orthopedic application: A review from a biological perspective. *J. Biomed. Mater. Res. Part B Appl. Biomater.* **2014**, *102*, 1316–1331.
4. Aghion, E.; Jan, L.; Meshi, L.; Goldman, J. Increased corrosion resistance of the AZ80 magnesium alloy by rapid solidification. *J. Biomed. Mater. Res. Part B Appl. Biomater.* **2015**, *103*, 1541–1548. [CrossRef] [PubMed]

5. Zhang, L.; Cao, Z.Y.; Liu, Y.B.; Su, G.H.; Cheng, L.R. Effect of Al content on the microstructures and mechanical properties of Mg–Al alloys. *Mater. Sci. Eng. A.* **2009**, *508*, 129–133. [CrossRef]
6. Taltavull, C.; Torres, B.; Lopez, A.J.; Rodrigo, P.; Otero, E.; Atrens, A.; Rams, J. Corrosion behaviour of laser surface melted magnesium alloy AZ91D. *Mater. Des.* **2014**, *57*, 40–50. [CrossRef]
7. Liu, C.; Liang, J.; Zhou, J.; Wang, L.; Li, Q. Effect of laser surface melting on microstructure and corrosion characteristics of AM60B magnesium alloy. *Appl. Surface Sci.* **2015**, *343*, 133–140. [CrossRef]
8. Taltavull, C.; Torres, B.; López, A.J.; Rodrigo, P.; Otero, E.; Rams, J. Selective laser surface melting of a magnesium–aluminium alloy. *Mater. Lett.* **2012**, *85*, 98–101. [CrossRef]
9. Yang, Y.; Wu, P.; Lin, X.; Liu, Y.; Bian, H.; Zhou, Y.; Gao, C.; Shuai, C. System development, formability quality and microstructure evolution of selective laser-melted magnesium. *Virtual Phys. Prototyp.* **2016**, *11*, 173–181. [CrossRef]
10. Xie, D.; Zhao, J.; Qi, Y.; Li, Y.; Shen, L.; Xiao, M. Decreasing pores in a laser cladding layer with pulsed current. *Chin. Opt. Lett.* **2013**, *11*, 54–57.
11. Ralston, K.D.; Birbilis, N. Effect of Grain Size on Corrosion: A Review. *Corrosion* **2010**, *66*, 319–324. [CrossRef]
12. Thijs, L.; Verhaeghe, F.; Craeghs, T.; Humbeeck, J.V.; Kruth, J.P. A study of the microstructural evolution during selective laser melting of Ti–6Al–4V. *Acta Mater.* **2010**, *58*, 3303–3312. [CrossRef]
13. Ding, Y.; Wen, C.; Hodgson, P.; Li, Y. Effects of alloying elements on the corrosion behavior and biocompatibility of biodegradable magnesium alloys: A review. *J. Mater. Chem.* **2014**, *2*, 1912–1933. [CrossRef]
14. Li, R.; Shi, Y.; Wang, Z.; Li, W.; Liu, J.; Wei, J. Densification behavior of gas and water atomized 316L stainless steel powder during selective laser melting. *Appl. Surf. Sci.* **2010**, *256*, 4350–4356. [CrossRef]
15. Song, B.; Dong, S.; Zhang, B.; Liao, H.; Coddet, C. Effects of processing parameters on microstructure and mechanical property of selective laser melted Ti6Al4V. *Mater. Des.* **2012**, *35*, 120–125. [CrossRef]
16. Wang, Z.; Guan, K.; Gao, M.; Li, X.; Chen, X.; Zeng, X. The microstructure and mechanical properties of deposited-IN718 by selective laser melting. *J. Alloys Compd.* **2012**, *513*, 518–523. [CrossRef]
17. Ng, C.C.; Savalani, M.M.; Lau, M.L.; Man, H.C. Microstructure and mechanical properties of selective laser melted magnesium. *Appl. Surface Sci.* **2011**, *257*, 7447–7454. [CrossRef]
18. Wei, K.; Gao, M.; Wang, Z.; Zeng, X. Effect of energy input on formability, microstructure and mechanical properties of selective laser melted AZ91D magnesium alloy. *Mater. Sci. Eng. A* **2014**, *611*, 212–222. [CrossRef]
19. Zhou, Y.; Wu, P.; Yang, Y.; Gao, D.; Feng, P.; Gao, C.; Wu, H.; Liu, Y.; Bian, H.; Shuai, C. The microstructure, mechanical properties and degradation behavior of laser-melted Mg–Sn alloys. *J. Alloys Compd.* **2016**, *687*, 109–114. [CrossRef]
20. El-Kady, O.; Fathy, A. Effect of SiC particle size on the physical and mechanical properties of extruded Al matrix nanocomposites. *Mater. Des.* **2014**, *54*, 348–353. [CrossRef]
21. Kokubo, T.; Takadama, H. How useful is SBF in predicting in vivo bone bioactivity? *Biomaterials* **2006**, *27*, 2907–2915. [CrossRef] [PubMed]
22. Gu, D.; Shen, Y. Balling phenomena in direct laser sintering of stainless steel powder: Metallurgical mechanisms and control methods. *Mater. Des.* **2009**, *30*, 2903–2910. [CrossRef]
23. Shuai, C.; Yang, Y.; Wu, P.; Lin, X.; Liu, Y.; Zhou, Y.; Feng, P.; Liu, X.; Peng, S. Laser rapid solidification improves corrosion behavior of Mg–Zn–Zr alloy. *J. Alloys Compd.* **2016**, *691*, 961–969. [CrossRef]
24. Gao, L.; Chen, R.S.; Han, E.H. Effects of rare-earth elements Gd and Y on the solid solution strengthening of Mg alloys. *J. Alloys Compd.* **2009**, *481*, 379–384. [CrossRef]
25. Jiqing, L.I.; Liu, Y.; Zhao, X.; Ruizhi, W.U. Effects of Al content on the lattice parameter and microstrain of α-Mg phase in Mg–Li alloys. *Appl. Sci. Technol.* **2011**, 501–504.
26. Kita, H.; Kimoto, M.; Kudo, T. Influence of Al Content on Corrosion Resistance of Mg–Al–Zn Alloys in Chloride Environments. *J. Jpn. Inst. Metals* **2005**, *69*, 805–809. [CrossRef]
27. Baker, J.C.; Gahn, J.W. Solute trapping by rapid solidification. *Acta Metall.* **1969**, *17*, 575–578. [CrossRef]
28. Kim, J.M.; Park, J.S. Effects of Grain Refinement and Melt Stirring on the Mechanical Properties and Fluidity of Mg–Al Alloys. *J. Korea Foundry Soc.* **2010**, *30*, 111–114.
29. Wen, Z.; Wu, C.; Dai, C.; Yang, F. Corrosion behaviors of Mg and its alloys with different Al contents in a modified simulated body fluid. *J. Alloys C ompd.* **2009**, *488*, 392–399. [CrossRef]
30. Ko, Y.J.; Chang, D.Y.; Lim, J.D.; Shin, K.S. Effect of $Mg_{17}Al_{12}$ Precipitate on Corrosion Behavior of AZ91D Magnesium Alloy. *Mater. Sci. Forum* **2003**, *419*, 851–856. [CrossRef]

31. Li, Z.; Gu, X.; Lou, S.; Zheng, Y. The development of binary Mg–Ca alloys for use as biodegradable materials within bone. *Biomaterials* **2008**, *29*, 1329–1344. [CrossRef] [PubMed]
32. Song, Y.; Shan, D.; Chen, R.; Zhang, F.; Han, E.H. Biodegradable behaviors of AZ31 magnesium alloy in simulated body fluid. *Mater. Sci. Eng C* **2009**, *29*, 1039–1045. [CrossRef]